



Hybrid 3D printed integrated microdevice for the determination of copper ions in human body fluids

Shuai Jiang¹ · Jie Zhao¹ · Shifan Zhao^{2,3} · Huizhen Deng¹ · Rui Zhu^{2,3} · Yujian Bai^{2,3} · Guofeng Cui^{2,3}

Received: 8 March 2022 / Revised: 24 March 2022 / Accepted: 28 March 2022 / Published online: 9 April 2022
© Springer-Verlag GmbH Germany, part of Springer Nature 2022

Abstract

On-site screening of copper ions in body fluid plays a critical role in monitoring human health, especially in heavy pollution areas. In this study, we have developed a hybrid 3D printed integrated microdevice for the determination of copper ions in human body fluids. A fixed and low volume of sample was detected by using the integrated microdevice without any pre-processing. The hybrid channel enables sample uniform mixing and quantitative dilution with buffer solution by inducing the “horseshoe vortex” phenomenon. The electrolytic microcell based on the flow detection system shows a more effective copper ion reaction ratio and, as a result, a better sensitivity. The simulation of the finite element method (FEM) determined the relevant optimum parameters of the hybrid channel and the microcell. The design, fabrication, and detection procedure of the integrated microdevice are here illustrated. The microdevice presented superior detection properties towards copper ions. The calibration curves covered two linear ranges varying from 20 to 100 ppb and 100 to 400 ppb, respectively. The limit of detection was estimated to be 15 ppb ($S/N=3$). The relative standard deviation of the peak current measurements was 2.26%. The designed microdevice was further applied to detect copper ions in practical samples (calf serum sample and synthetic human urine sample) using a standard addition method, and the average recovery was found to be 95–104%. The performance of copper ion detection with the integrated microdevice was consistent with that of the inductively coupled plasma mass spectrometry (ICP-MS) in the same practical samples, demonstrating significant practicality in the test of body fluids. The portable integrated microdevice is an excellent choice for on-site detection and has a promising prospect in the point-of-care testing (POCT) applications.

Keywords Integrated microdevice · Hybrid channel · Flow detection · Copper ions · COMSOL

Introduction

While the advances in industrialization and technology have provided convenience and benefits to human life in recent decades, it concurrently entailed heavy metal pollution to the ecosphere. Excessive heavy metals will accumulate through the food chain and reach the human body eventually, posing

a grave threat to humankind’s health [1–3]. Cu, for instance, is an essential heavy metal element that acts as a cofactor of numerous proteins and enzymes, and widely participates in metabolic processes and vital movement [4]. Consequently, the range of Cu ion concentrations is very strictly controlled. Wilson’s disease, Menkes disease, heart and renal failure, brain and kidney damage, liver damage, and even mortality have all been linked to high copper levels in the human body [5–8]. Copper ions in the blood are often found at concentrations of 1 to 1.5 ppm [9]. Urination is the primary method of excreting heavy metal and detoxifying when it surpasses the usual concentration. Copper excretion in the urine is only around 95 ppb in general, but it can reach 636 ppb in those with Wilson’s disease [10]. As a result, the determination of copper ions in body fluids (blood and urine) is a simple and effective preliminary diagnostic test, which helps in assessing one’s degree of heavy metal exposure as well as supports follow-up therapy studies [11, 12].

✉ Jie Zhao
zhaoj77@scut.edu.cn

¹ School of Mechanical and Automotive Engineering, South China University of Technology, Guangzhou 510640, People’s Republic of China

² School of Chemistry, Sun Yat-Sen University, Guangzhou 510275, People’s Republic of China

³ Key Laboratory of Low-Carbon Chemistry & Energy Conservation of Guangdong Province, Sun Yat-Sen University, Guangzhou 510275, People’s Republic of China

According to the World Health Organization, affordable and convenient device for heavy metal detection on-site is still in major shortage, particularly in low-income regions [13]. Traditional heavy metal analysis methods, such as atomic absorption spectroscopy (AAS) and inductively coupled plasma mass spectrometry (ICP-MS), need bulky, costly analytical instruments and professional operational skills [14, 15]. Benefiting from the effective deposition process and the advanced electrochemical measurements, square wave anodic stripping voltammetry (SWASV) becomes the most sensitive and powerful electroanalytical tool for the trace-level determination of heavy metals [16, 17]. Conventional SWASV, on the other hand, suffers from high reagent use, poor reproducibility, and instability [18, 19]. Microfluidics, also known as lab-on-a-chip (LOC), has aroused people's great interest, particularly during the difficult times of the COVID-19 pandemic, for its numerous advantages, such as precise control and manipulation of low-volume fluids, reduced reagent consumption, lowered detection time, higher sensitivity and detection automation [20–24]. Integrated LOC devices, such as centrifugal microfluidics devices, can incorporate many of the necessary functionality of biochemistry and medical analysis field into a tiny chip [25–27]. The flow detection system with SWASV based on microfluidics has been investigated [28–30]. The flow detection system can ensure that the fresh solution flows across the electrode surface, increasing the accumulation efficiency. Furthermore, electrodes inserted in the microdevice help prevent external damage or disturbance [31]. However, a single “flow cell” still lacks necessary sample preprocessing steps like mixing and dilution, and extra external corollary equipment like wastewater bottles will add the complexity of the detection procedure. Hence, the integration of microfluidics and flow detection system helpfully tackles these shortcomings and is engaged as an ideal development trend for the next generation of point-of-care testing (POCT) systems [32, 33].

The finite element method (FEM) has become an indispensable and trustworthy tool in practically all research and application fields due to its low cost and great manufacturing efficiency [34]. It supplies great help in analyzing, amending, optimizing, and evaluating designing processes [35, 36]. Three-dimensional (3D) printing, in contrast to expensive microfluidic device manufacturing techniques such as soft lithography and nanofabrication, simply requires low-cost raw material and lax limits on professional skills, and stereolithography is the most promising of these technologies [37–40]. Therefore, we used 3D printing to manufacture our proposed microdevice based on the simulation results.

In this paper, we report a single-use, portable hybrid 3D printed integrated microdevice for detecting copper ions in human body fluids (as shown in Fig. 1). The microdevice is consisted of two parts: an arc-shaped serpentine

microchannel with multi dam structure designed for homogeneous sample/buffer mixing and dilution, an electrochemical microcell developed for efficient Cu^{2+} deposition and stripping during SWASV detection. In addition, both the microchannel and the microcell parameters were optimized and confirmed using the FEM software. The microdevice integration involves the incorporation of external commercial electrodes. The choice of working electrode plays a crucial role in stripping analysis. The Au electrode is an ideal candidate for Cu stripping because of its efficient deposition, sensitive redox reaction of target ion, excellent biocompatibility, and other features [41]. The integrated microdevice was further demonstrated to detect copper ions presented in standard solutions as well as practical samples. The electrochemical detection results were consistent with those obtained from ICP-MS. The integrated microdevice's superior analytical properties and straightforward detection procedure make it a viable option in the POCT applications.

Materials and methods

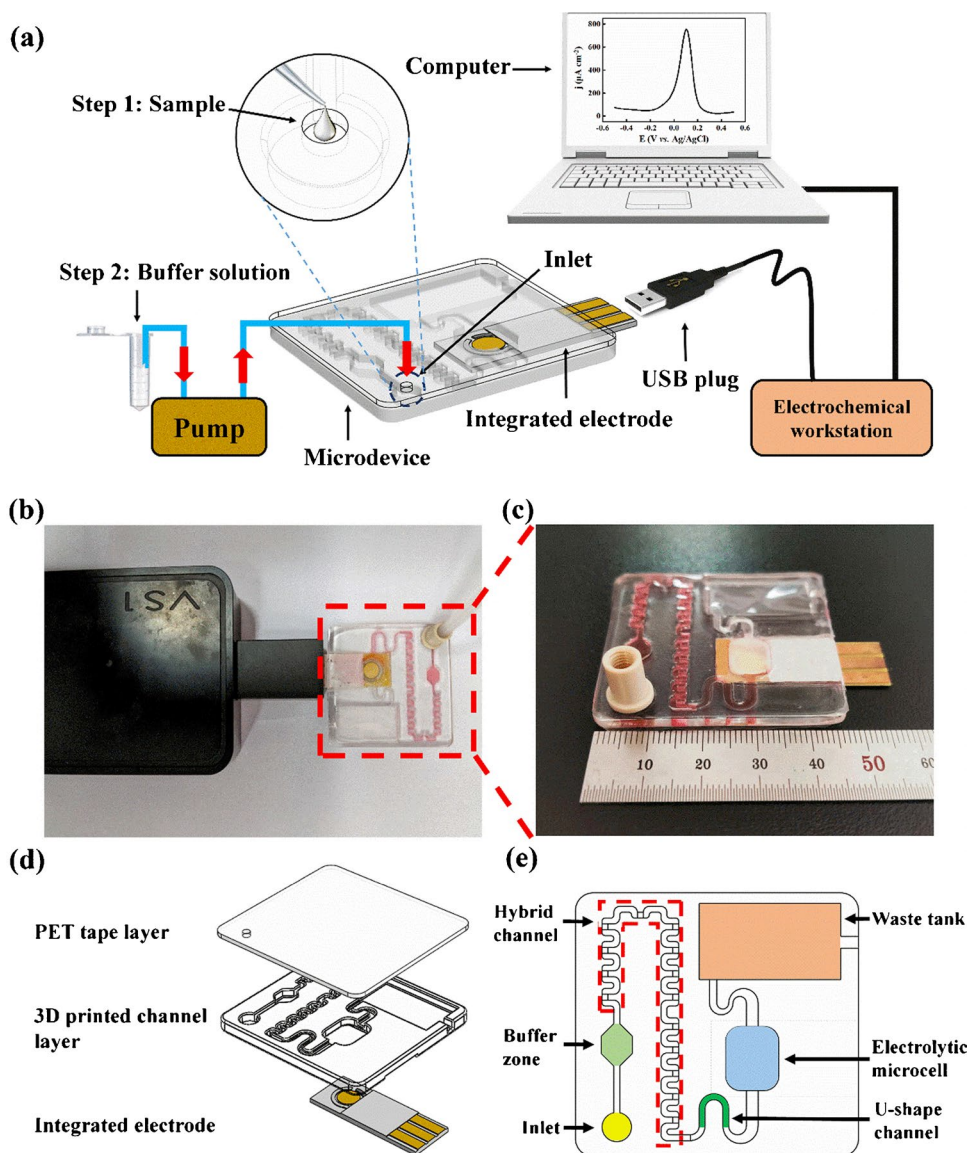
Reagents and solutions

CH_3COOH , $\text{CH}_3\text{COONa}\cdot 3\text{H}_2\text{O}$, and $\text{CH}_3\text{CH}_2\text{OH}$ were obtained from Aladdin Company (Shanghai, China). $\text{Cu}(\text{NO}_3)_2$ was purchased from Xilong Chemical Co., Ltd. (Guangzhou, China). The standard solution of Cu^{2+} was prepared by dissolving and diluting $\text{Cu}(\text{NO}_3)_2$. Calf serum samples were purchased from Maigen Technology Co., Ltd. (Guangzhou, China). The synthetic urine samples were purchased from Beijing Solarbio Science & Technology Co., Ltd. (Beijing, China). All samples were stored at $-20\text{ }^\circ\text{C}$ until used. The commercial three electrodes were purchased from Mecart Sensor Technology Co., Ltd. (Guangzhou, China). The electrode's precise dimensions were clearly displayed (see ESM Fig. S1). The working electrode was Au, and Pt and Ag/AgCl were used as counter electrode and reference electrode, respectively. All the three electrodes were prepared externally. Before the experiment, the three electrodes were cleaned with acetone, absolute ethanol, and deionized water sequentially, and then dried in a $60\text{ }^\circ\text{C}$ oven for 15 min. All aqueous solutions were prepared with deionized water purified via a Millipore water purification system (resistivity $> 18.3\text{ M}\Omega\text{ cm}$) throughout the experiment, and all the chemicals were of analytical grade, which can be used without further purification.

Design and fabrication of the integrated microdevice

As illustrated in Fig. 1d, the designed integrated microdevice includes a multi-layer structure, a single-sided PET adhesive

Fig. 1 **a** Schematic diagram of the microdevice system, consisting of (1) the 3D printed microdevice; (2) a peristaltic pump; (3) an integrated electrode; (4) an electrochemical workstation; and (5) a computer. **b** The photo of the microdevice system. **c** The enlarged photo of the microdevice. The dimensions of the microdevice: 48 mm length \times 45 mm width \times 3 mm height. **d** The exploded view of the integrated microdevice. **e** The detailed composition of 3D printed channel layer



tape layer, a 3D printed channel layer, and a piece of integrated gold electrode. There are six parts in the 3D printed channel layer, including inlet, buffer zone, hybrid channel, U-shape channel, electrolytic microcell, and waste tank, see Fig. 1e.

The channel layer was manufactured using the stereolithography method. The microchannel structure was first designed using SolidWorks software 2019 (Concord, MA, USA) and then printed using the PolyJet 3D printing system (UnionTech lite 600, UnionTech company). SOMOS Water-Clean Ultra 10122 photosensitive resin was used as the raw material of 3D printing from stereo lithography appearance prototyping. The total fabrication cost was less than 2 US dollars, which was cheaper than other microdevice fabrication method. The contact angle is an important characterization of the 3D printing materials. The contact angle was

measured by pipetting a 10- μ L droplet of ultrapure water on the fabricated microdevice. An image of the droplet was taken from the side, and the contact angle was calculated directly using the image processing software ImageJ (NIH, USA). The contact angle was approximately 46°, which proved good hydrophilicity of the fabricated microdevice (see ESM Fig. S2).

After fabrication, the channel layer was cleaned with deionized water and dried in a 40 °C oven for 30 min. The top of the channel layer was then sealed using 3 M™ PET 851 J tape (3 M Company, USA) to prevent leaking. There is an electrode groove that corresponds to the size of the three electrodes on the bottom of the channel layer (see ESM Fig. S3). During the assembly, the commercial three electrodes were properly fitted into the groove, and any possible cracks were repaired with adhesive. After the whole

assembly, diluted red ink was injected into the microcell to check for leaks in the integrated microdevice. Due to the delicate construction and relatively high transparency of the device, a 3D digital microscope (3DM-02, Teelen Optical) was used to monitor the flow inside real time during the experiment.

Copper ion assay protocol using the integrated microdevice

Figure 1a depicts the whole sample preprocessing and analyte detection protocol utilizing the integrated microdevice. The inlet of integrated microdevice was connected with a peristaltic pump (BT100-2 J, Longer Pump Instrument) through an inner diameter of a 0.8-mm hose and the three electrodes were linked with an electrochemical workstation via a USB plug. Deionized water was pumped into the microdevice before each test to clean it, and then, a large amount of air was pumped into it to dry it. The wastewater was discharged through the waste tank outflow.

In each test, 50 μL of test standard solution was injected into the inlet of the microdevice by using a pipette, followed by 3 mL of 0.1 M acetate buffer solution (ABS, pH=5.5). A preliminary mixing of the sample and buffer solution would take place in the buffer zone. Meanwhile, the buffer zone can help to mitigate the effects of the pump's cyclical fluctuation. The two distinct kinds of solutions were then mixed and diluted uniformly in the hybrid channel. The mixing time to flow through the hybrid channel was 20 s. After the diluted sample was gradually delivered into the electrolytic microcell and the whole microcell was filled, the integrated electrode started to pre-deposit for 60 s. The three electrodes conducted anodic stripping after a 10-s equilibration period, and the current signal was transferred to the electrochemical workstation through a USB. Finally, the wastewater flowed into the waste tank. The U-shape channel prevented probable liquid backflow throughout the detection procedure, and the peristaltic pump powered the fluid flow and maintained a constant flow velocity of 1.0 mL/min. The entire detecting process took less than 2 min. All SWASV measurements were performed using a CHI660C electrochemical workstation (CH Instruments, Chenhua Co., Shanghai, China) with the deposition potential of -1.2 V, the frequency of 40 Hz, the amplitude of 30 mV, and the potential increment step of 4 mV.

The presented integrated microdevice is single-use and convenient. The waste tank inside the microdevice can collect wastewater after an experiment, preventing the contamination of biological materials in the external environment and possible cross-infection. To save money on the following test, wastewater was evacuated and the microdevice was cleansed with deionized water in the real trial.

Results and discussion

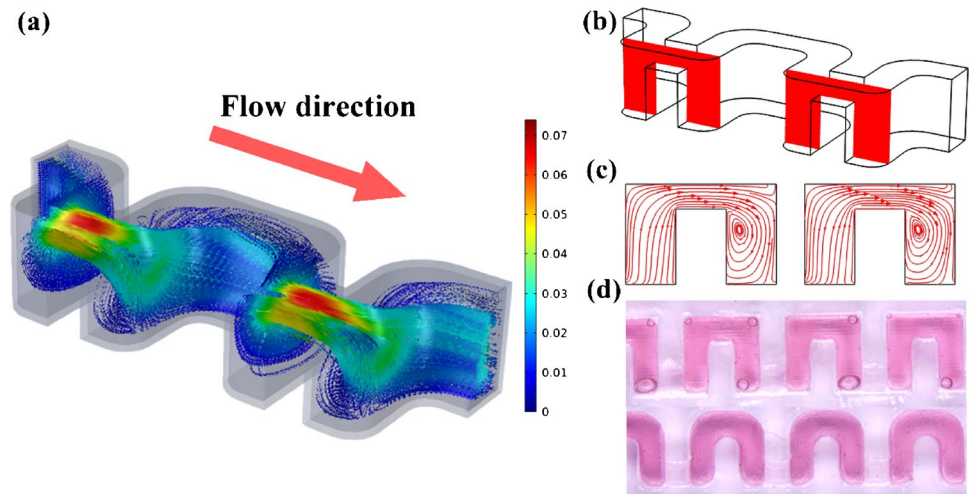
Simulation and characterization of the hybrid channel

To evaluate the mixing impact of the hybrid channel in the microdevice, the flow velocity pattern inside the hybrid channel was numerically simulated using the commercial FEM software COMSOL Multiphysics 5.3a (Burlington, MA, USA). Assuming a condition of laminar incompressible flow, the “Laminar Flow” module was used to model the sample flow. The Navier–Stokes (N-S) equation (Eq. 1) was employed here.

$$\rho \left(\frac{\partial u}{\partial t} + u \cdot \nabla u \right) = -\nabla p + \mu \nabla^2 u \quad (1)$$

where ρ denotes the fluid density, μ represents the dynamic viscosity, u is the flow velocity, and p denotes the pressure. The physical properties of water were applied to the fluid in the model (dynamic viscosity $\mu = 1 \times 10^{-3}$ Pa s, density $\rho = 1000$ kg/m³). Since the dam structure is periodically arranged along the serpentine channel, only one unit of the channel (consisting of three curves and two dam structures) was simulated to decrease the computing burden. The dimension of the cross section of the inlet channel was 1.00 mm width \times 2.00 mm height, and the height of the dam structure was 1.50 mm (see ESM Fig. S4). The boundary condition velocity at the inlet side was set to be 0.010 m/s, while the static pressure at the outlet side was set to be zero. Figure 2a shows the 3D flow streamline profile, and Fig. 2b shows the specific cross section as well as the velocity arrow field in the plane (see Fig. 2c). The maximum velocity (0.076 m/s) was found in the narrow channel above the dam structure. As shown in Fig. 2c, the vortexes were found at the right side of the cross section of the curved channel, which was consistent with previous research [28]. The reason for this phenomenon is called the “horseshoe vortex” effect, in which a uniform flow passes through a narrow region and sudden spatial or direction variation leads to squash and stretch of fluid, which results in a dramatic vortex flow [42, 43]. Here, the relation between the maximum velocity and inlet velocity/dam height was briefly studied (see ESM Table S1). The dam height was found to have a more perceptible impact on the maximum velocity and the “horseshoe vortex.” Actually, there was no vortex when the dam height was 1.2 mm in our simulation. Overall, the simulation consequence indicates that the microchannel has a satisfactory mixing effect with a diverse variety of solutions. In addition, to describe the real mixing scenario, diluted red ink was used to replace the sample, as shown in Fig. 2d. In comparison to the previously published rectangular serpentine channel [44], the given arc-shaped construction aids in the elimination of bubbles or

Fig. 2 Finite element simulation and practical test of the designed hybrid channel. **a** The 3D flow streamlines profile of one unit of the serpentine microchannel. **b** The chosen cross section. **c** The detailed velocity arrow in the plane. **d** Picture of mixing effect in the rectangle serpentine channel and the arc-shaped serpentine channel



“dead zones,” hence reducing reagent use and lowering the possibility of detection interference.

Design and simulation of the electrolytic microcell

A single saddle-shaped microcell was designed to minimize the dead volume and avoid any reagent residue (see ESM Fig. S5). A model of the electrolytic microcell for the electrochemical detection of copper ions was built and simulated by using the FEM. Considering the fixed diameter of the commercial three electrodes, a 2D simulation was selected to simplify the calculation. Homoplastically, it was found that 2D simulation had greater accuracy than 3D simulation in previous research [45]. This microcell model demonstrated the impact of convection and diffusion on the transport-limited electrodeposition on the electrode surface. The microcell was running at a high overpotential so the predeposition rate was governed by the transport rate of the copper ion in the electrolyte. A result of this operating condition was that the electric potentials in the electrolyte and electrode need not be modeled to determine the current distribution on the electrode surface [46]. The microcell structure was completed in small geometries, so the liquid flow velocity was on the level of several millimeters per second, generally low Reynolds number. Consequently, as mentioned in the “Simulation and characterization of the hybrid channel” section, the N-S equation (as shown in Eq. 1) was employed. Because the sample is required to be adequately diluted, the transport of copper ions can be described using Fick’s second law:

$$\frac{\partial c}{\partial t} = D\nabla^2 c - u \cdot \nabla c \quad (2)$$

where D is the diffusion coefficient of species and c is the concentration of species. Use the “Transport of Diluted Species” module coupled to the flow velocity in the “Laminar Flow” module to model the mass transport. The diffusion

coefficient of the copper ion transport was set to $5 \times 10^{-10} \text{ m}^2/\text{s}$ by consulting previous literature [47]. Besides, the fluxes of the copper ion in combination with Faraday’s law can be used to calculate the local current density (i_{loc}) on the electrode surface:

$$i_{loc} = nFN_{Cu} \quad (3)$$

where n is the number of electrons in the electrode reactions, F is Faraday’s constant, and N_{Cu} is the normal flux of copper ions over the electrode surface.

A computational module with the working electrode (WE) domain is depicted in Fig. 3a, with the leftmost end

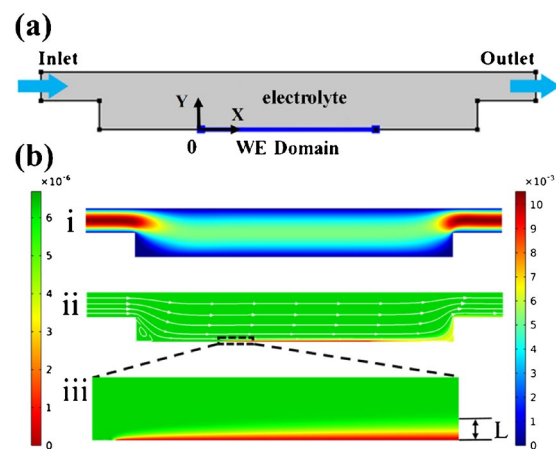


Fig. 3 **a** The computational module of microcell with the working electrode (WE) domain. **b** The velocity profiles (i), concentration profiles (ii) in microcell, and the partial enlarged drawing (iii) on the electrode surface. L means the thickness of diffusion layer. The depth of the microcell is 1.0 mm, the initial velocity is 0.007 m/s, and the initial concentration is $6 \times 10^{-6} \text{ mol/L}$

of the electrode serving as the origin of the coordinate axes. Because the counter electrode and reference electrode have little effect on the simulation, the model primarily focuses on the working electrode. The velocity profile and concentration profile of the microcell module are described in Fig. 3b. During the simulation, the fluid velocity at the inlet was found to be identical with the previously reported simulation [28], and the no-slip boundary condition was employed at the walls. The partially enlarged drawing of the concentration profile on the electrode surface and the distance of the concentration varying from zero to bulk are shown in Fig. 3b(iii).

The thinner diffusion layer and higher absolute deposition current density can improve the ions' efficient reaction on the electrode surface. To evaluate the deposition efficiency of copper ions in the microcell, the value of the diffusion layer thickness and Faraday current density in different parameters were compared. The significant influence factors (e.g., the microcell depth and fluid velocity) were investigated. First, the thickness of diffusion layer of various depths was studied under the same flow velocity (0.010 m/s). When demonstrated in Fig. 4a, the thickness exhibits a minor tendency to become thin as the depth of the microcell decreases from 1.40 to 0.60 mm over an equivalent distance. Contrarily, the effect of velocity was evaluated at the same height (1.0 mm). When demonstrated in Fig. 4b, the thickness of the diffusion layer decreases significantly (from 0.237 to 0.140 mm) as the velocity increases (from 0.003 to 0.023 m/s). Similarly, with

the same initial condition, the Faraday current density rises with either a decrease in microcell depth or the increase in the fluid velocity, while there are large gaps between different velocities in Fig. 4c and d. Consequently, the velocity has a far greater impact on the thickness of diffusion layer and Faraday current density than the microcell depth. Overall, the low microcell depth and the high flow velocity can help improve the detection performance of microcell; nevertheless, the microcell depth of 1.0 mm was chosen due to the commercial practical manufacturing limitations.

Optimization of conditions for copper ion detection

The stripping voltammetric peak currents for standard solutions of copper ion were recorded as the flow rate increased from 0.7 to 1.3 mL/min by 0.1 mL/min each time. The concentration of the diluted test sample was 300 ppb, and the SWASV parameters were the same as in the "Copper ion assay protocol using the integrated microdevice" section. As shown in Fig. 5a, the stripping voltammetric peak current was found to be increased with the increased flow rate and maximum peak current was found with the flow rate of 1.0 mL/min (0.008 m/s). This tendency was found to remain in our simulation in the "Design and simulation of electrolytic microcell" section because the flow predeposition allows fresh samples to replenish the consumption of copper ions deposited on the electrode surface in time, which alleviates the concentration polarization and improves the reaction

Fig. 4 Relationship between microcell depth and diffusion layer thickness (a); Faraday current density (c) resulting from FEM simulation respectively in the velocity of 0.010 m/s. Relationship between flow velocity and diffusion layer thickness (b); Faraday current density (d) respectively in the microcell depth of 1.0 mm

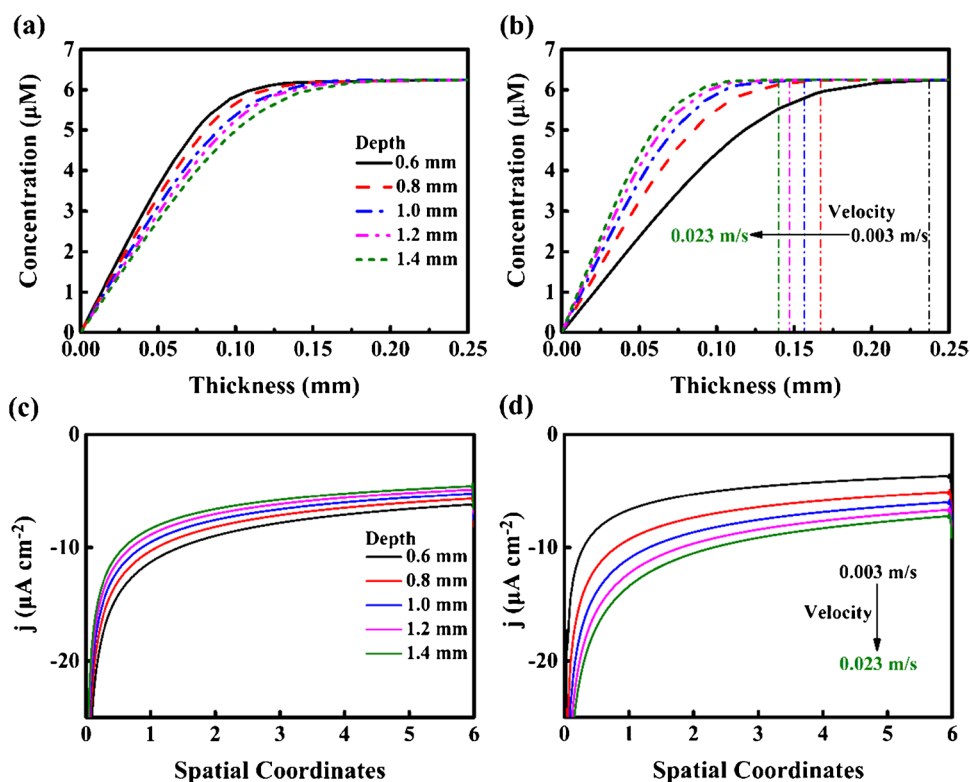
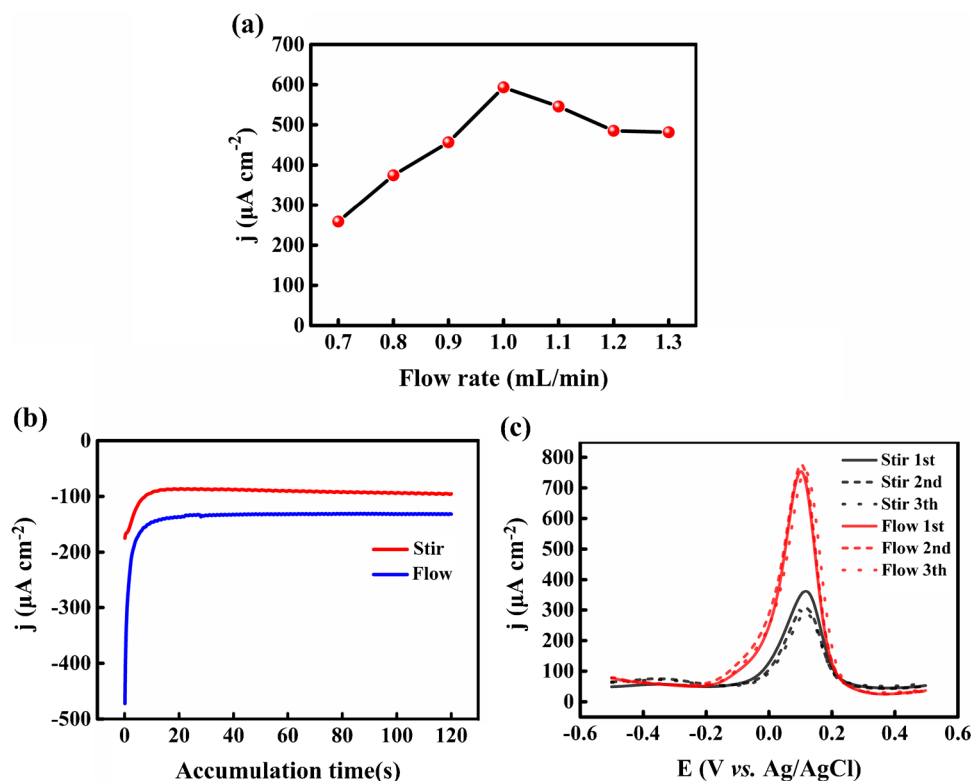


Fig. 5 **a** Influence of the flow rate on the stripping voltammetric current of Cu^{2+} (300 ppb). Accumulation **b** *i-t* curves and stripping voltammetric **c** *i-E* curves of Cu^{2+} (400 ppb) obtained using the stirring beaker system (stir) and the flowing microcell system (flow)



efficiency on the electrode surface, whereas the peak current was found to be decreased with the further increased flow rate. Two reasons can be used to explain this phenomenon: the first reason may be due to the overspeed flow which washed off the unstable deposited copper on the electrode; the second one is the development of vortices at the corner of upstream sides when the flow rate was over-quick in simulation, disrupting the ion deposition near the corner (see ESM Fig. S6). Thus, each structure with different parameters has its optimal flow rate. For further research on the microdevice, a flow rate of 1.0 mL/min was adopted.

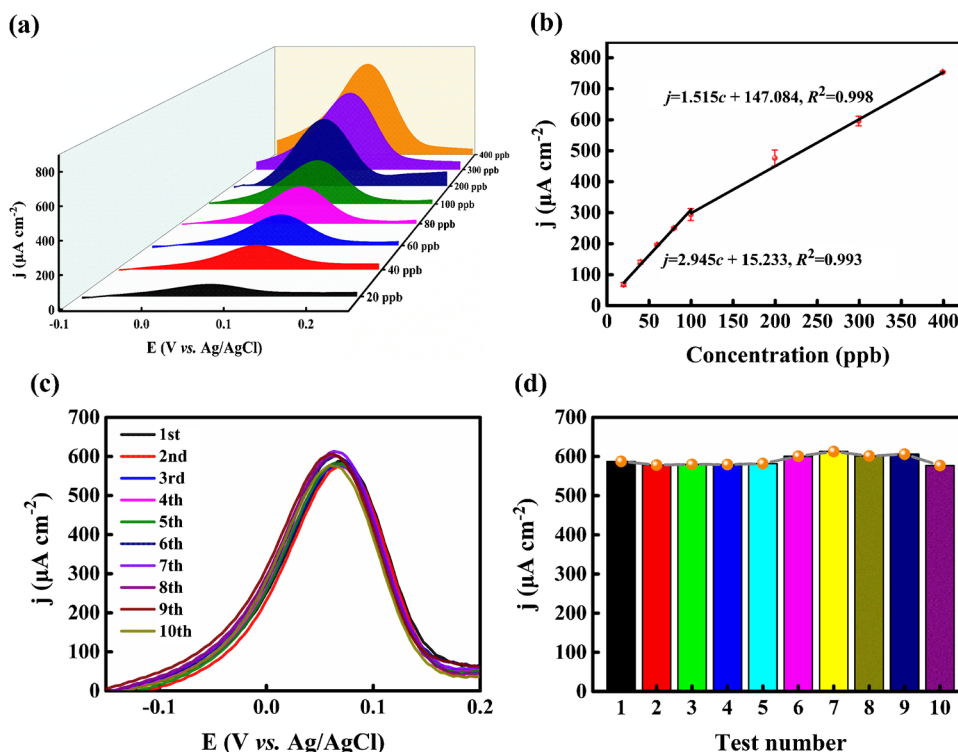
For comparison, the following studies were carried out using two alternative preconcentration procedures. The first method was using a conventional system by stirring 20 mL of sample in a beaker, and the second one was to drive the sample through the electrolytic microcell at the chosen flow rate (1.0 mL/min). Figure 5b and c show the comparison results of deposition *i-t* curves and stripping voltammetric *i-E* curves of Cu^{2+} (400 ppb) respectively obtained from the stirring beaker system and flowing microcell system. Both absolute accumulation current density (see Fig. 5b) and the stripping peak current density (see Fig. 5c) from the flowing microcell system were found to be greater than that obtained with the stirring beaker system. The microcell system with constant fluid continually flowing over the electrode surface ensured a steady accumulation state and smoother accumulation current curve. However, the traditional stirring beaker system might result in an unstable solution and current

fluctuation. Meanwhile, as indicated in the earlier simulation, a high flow rate could reduce the thickness of diffusion layer and increase the effective reaction ratio between the electrode surface and copper ions. Besides, compared with the stirring beaker system, which requires a large volume of sample and buffer solution, the microcell volume is around 150 μL and the sample volume can be as low as 50 μL , and the total buffer solution consumption of each test is less than 4 mL. In terms of stability, sensitivity, and test cost, the data above clearly showed that the flowing microcell system outperformed the conventional beaker system.

Assessment of determination performance

Under the optimum conditions of the integrated microdevice, standard solution of Cu^{2+} with different concentrations was tested and the stripping voltammetric *i-E* curves were obtained, and the results are shown in Fig. 6a and b. The potential of Cu^{2+} in the stripping peak was found to be 0.1 V. Two linear ranges are varying from 20 to 100 ppb and 100 to 400 ppb respectively with a deposition potential of -1.2 V and a deposition time of 60 s. The correlation equations were fitted as $j = 2.945c + 15.233$ ($\mu\text{A/cm}^2$) with a correlation coefficient of 0.993 in the range of 20 to 100 ppb, and as $j = 1.515c + 147.084$ ($\mu\text{A/cm}^2$) with a correlation coefficient of 0.998 in the range of 100 to 400 ppb. Moreover, a detection limit of 15 ppb was achieved ($S/N=3$). This linear range

Fig. 6 **a** Stripping voltammetric *i*-*E* curves of standard solutions of Cu^{2+} with concentrations in the range of 20 ppb – 400 ppb and **b** the linear calibration curves. **c** Ten replicated stripping voltammograms and **d** corresponding peak height continuously recorded with the integrated microdevice



and detection limit can well meet the detection requirement of Cu^{2+} in practical body fluids.

The reproducibility of the fabricated microdevice for stripping analysis of Cu^{2+} was examined by recording the stripping voltammograms under the same condition mentioned above in a solution containing 300 ppb copper ion. Ten continuous stripping voltammetric *i*-*E* curves and the corresponding peak height for Cu^{2+} determination using the same Au integrated electrode can be found in Fig. 6c and d. The relative standard deviation (RSD) of the peak measurements was calculated to be 2.26%. The integrated microdevice we designed has great repeatability thanks to the fixed electrode spacing, consistent flow rate, and the whole microfluidics structure that isolates outside small disturbance.

Practical sample analysis

The performance of on-site monitoring of the microdevice was evaluated by determining copper ions in different practical samples. The detection was performed under optimum experimental conditions using the standard addition method, and the results were compared to data from the ICP-MS analysis of the identical samples. In detail, the test practical samples were firstly prepared by adding different concentrations of Cu^{2+} in the blank practical sample. A 50- μL droplet of test practical sample was injected into the inlet, and then, 3 mL of 0.1 M ABS (pH = 5.5) was pumped into the microdevice. The deposition period was kept at 60 s to minimize the peak distortion and current attenuation because

of protein-adherent contamination in the sample (see ESM Fig. S7). The oxidation peak current density was measured by SWASV at the oxidation potential of Cu^{2+} (see ESM Fig. S8). The concentrations of Cu^{2+} were obtained from the calibration plot. This procedure was repeated three times for each sample. The results of the determination of copper ions in the test sample are presented in Table 1. The electrochemical detection results were consistent with those obtained from the ICP-MS analysis. The relative standard deviation (RSD) was less than 5% and the recovery was between 95 and 104%. Such results indicated that the presented integrated microdevice possessed the reliability and immense potential for the detection of Cu^{2+} in human body fluids.

Conclusion

In this paper, a hybrid 3D printed integrated microdevice has been successfully designed and fabricated for determining copper ions in human body fluids by using SWASV. The microdevice is capable of fast and convenient determination of copper ions in the practical sample without any preprocessing. The hybrid channel inside the microdevice provided a uniform sample mixing and dilution with buffer solution. The microcell with flow detection mechanism exhibited high sensitivity and excellent reproducibility towards the copper ion determination. The characteristics of the hybrid channel and microcell were optimized and confirmed using FEM modeling. Considering the actual

Table 1 Determination of copper ions in serum and urine sample ($N=3$)

Sample	Spiked concentration (ppb)	Found result (ppb)	RSD (%)	Recovery (%)	ICP-MS (ppb)
Serum	0	–	–	–	2.29
	100	103.4	2.61	103.4	102.3
	200	197.6	2.43	98.8	208
	300	287.3	4.46	95.8	316
Urine	0	–	–	–	–
	100	102.1	2.03	102.1	101.6
	200	205.7	1.93	102.9	203
	300	298.5	2.55	99.5	307

– not detected

manufacture and detection, the microcell depth of 1.0 mm and the fluid velocity of 1.0 mL/min (0.008 m/s) were the optimum parameters. The developed integrated microdevice enabled copper ion determination in the range 20 to 400 ppb, with a limit of detection of 15 ppb. The detection results of copper ions by using the integrated microdevice were comparable to the results by ICP-MS in the same practical samples, which demonstrate great feasibility in the practical test of body fluids. The integrated microdevice is also more economical and available because of the low-cost 3D printing manufacturing technique and straightforward assembly processes. The single-use mechanism based on the waste tank prevents the contamination of biological samples to the external environment. The hybrid 3D printed integrated microdevice has broad prospects in on-site detection of copper ions in the backward areas suffering heavy metal pollution, and provides a new perspective for the POCT applications.

Supplementary Information The online version contains supplementary material available at <https://doi.org/10.1007/s00216-022-04049-9>.

Author contribution Shuai Jiang: conceptualization, investigation, methodology, data collection, data curation, writing, editing, visualization. Jie Zhao: conceptualization, supervision, methodology, writing, editing. Shifan Zhao: supervision, writing—review and editing, visualization. Huizhen Deng: methodology, data curation, editing. Rui Zhu: methodology, data curation, writing. Yujian Bai: data collection, data curation. Guofeng Cui: conceptualization, methodology, supervision, funding acquisition.

Funding Dr. J. Zhao and G. Cui gratefully acknowledge the financial support by National Natural Science Foundation of China (51571093, 51271205), “Tian’e Plan” by Huizhou city (20170220011822281, 20170220085037390). Dr. G. Cui and S. Zhao acknowledge funding received from the Scientific Technology Project of Guangzhou City (202103000003).

Data availability Not applicable.

Code availability Not applicable.

Declarations

Ethics approval All applicable international, national, and/or institutional guidelines for the care and use of animals were followed. Calf serum samples were purchased from commercial blood product corporation rather than collected specifically for this study.

Conflict of interest The authors declare no competing interests.

References

- Huang H, Chen T, Liu X, Ma H. Ultrasensitive and simultaneous detection of heavy metal ions based on three-dimensional graphene-carbon nanotubes hybrid electrode materials. *Anal Chim Acta*. 2014;852:45–54. <https://doi.org/10.1016/j.aca.2014.09.010>.
- Li M, Gou H, Al-Ogaidi I, Wu N. Nanostructured sensors for detection of heavy metals: a review. *ACS Sustain Chem Eng*. 2013;1(7):713–23. <https://doi.org/10.1021/sc400019a>.
- Sud D, Mahajan G, Kaur MP. Agricultural waste material as potential adsorbent for sequestering heavy metal ions from aqueous solutions - a review. *Bioresour Technol*. 2008;99(14):6017–27. <https://doi.org/10.1016/j.biortech.2007.11.064>.
- Hui X, Sharifuzzaman M, Sharma S, Xuan X, Zhang S, Ko SG, et al. High-performance flexible electrochemical heavy metal sensor based on layer-by-layer assembly of $Ti_3C_2T_x$ /MWNTs nanocomposites for noninvasive detection of copper and zinc ions in human biofluids. *ACS Appl Mater Interfaces*. 2020;12(43):48928–37. <https://doi.org/10.1021/acsmi.0c12239>.
- Ahmad W, Alharthy RD, Zubair M, Ahmed M, Hameed A, Rafique S. Toxic and heavy metals contamination assessment in soil and water to evaluate human health risk. *Sci Rep*. 2021;11(1):17006. <https://doi.org/10.1038/s41598-021-94616-4>.
- Fraga CG. Relevance, essentiality and toxicity of trace elements in human health. *Mol Aspects Med*. 2005;26(4–5):235–44. <https://doi.org/10.1016/j.mam.2005.07.013>.
- Fu X-C, Wu J, Li J, Xie C-G, Liu Y-S, Zhong Y, et al. Electrochemical determination of trace copper(II) with enhanced sensitivity and selectivity by gold nanoparticle/single-wall carbon nanotube hybrids containing three-dimensional l-cysteine molecular adaptors. *Sens Actuator B-Chem*. 2013;182:382–9. <https://doi.org/10.1016/j.snb.2013.02.074>.
- Schaefer M, Schellenberg M, Merle U, Weiss KH, Stremmel W. Wilson protein expression, copper excretion and sweat

- production in sweat glands of Wilson disease patients and controls. *BMC Gastroenterol.* 2008;8:29. <https://doi.org/10.1186/1471-230X-8-29>.
9. Wang Q, Li T, Fang D, Li X, Fang L, Wang X, et al. Micromotor for removal/detection of blood copper ion. *Microchem J.* 2020; 158. <https://doi.org/10.1016/j.microc.2020.105125>.
 10. Procházková S, Halko R. Determination of copper in human urine by cloud point extraction and flame atomic absorption spectrometry. *Anal Lett.* 2016;49(11):1656–68. <https://doi.org/10.1080/00032719.2015.1120740>.
 11. Bagheri N, Mazzaracchio V, Cinti S, Colozza N, Di Natale C, Netti PA, et al. Electroanalytical sensor based on gold-nanoparticle-decorated paper for sensitive detection of copper ions in sweat and serum. *Anal Chem.* 2021;93(12):5225–33. <https://doi.org/10.1021/acs.analchem.0c05469>.
 12. Gao W, Nyein HYY, Shahpar Z, Fahad HM, Chen K, Emaminejad S, et al. Wearable microsensor array for multiplexed heavy metal monitoring of body fluids. *ACS Sensors.* 2016;1(7):866–74. <https://doi.org/10.1021/acssensors.6b00287>.
 13. McNerney R. Diagnostics for Developing Countries. *Diagnostics.* 2015;5(2):200–9. <https://doi.org/10.3390/diagnostics5020200>.
 14. Müller W, Iffland R. Studies on metals in meningiomas by atomic absorption spectrometry. *Acta Neuropathol.* 1981;55(1):53–8. <https://doi.org/10.1007/BF00691531>.
 15. Park YM, Choi JY, Nho EY, Lee CM, Hwang IM, Khan N, et al. Determination of macro and trace elements in canned marine products by inductively coupled plasma—optical emission spectrometry (ICP-OES) and ICP-mass spectrometry (ICP-MS). *Anal Lett.* 2018;52(6):1018–30. <https://doi.org/10.1080/00032719.2018.1510938>.
 16. Nolan MA, Kounaves SP. Microfabricated array of iridium microdisks as a substrate for direct determination of Cu^{2+} or Hg^{2+} using square-wave anodic stripping voltammetry. *Anal Chem.* 1999;71(16):3567–73. <https://doi.org/10.1021/ac990126i>.
 17. Pizarro J, Flores E, Jimenez V, Maldonado T, Saitz C, Vega A, et al. Synthesis and characterization of the first cyrhetrenyl-appended calix[4] arene macrocycle and its application as an electrochemical sensor for the determination of Cu(II) in bivalve mollusks using square wave anodic stripping voltammetry. *Actuator B-Chem.* 2019;281:115–22. <https://doi.org/10.1016/j.snb.2018.09.099>.
 18. Ratner N, Mandler D. Electrochemical detection of low concentrations of mercury in water using gold nanoparticles. *Anal Chem.* 2015;87(10):5148–55. <https://doi.org/10.1021/ac504584f>.
 19. Zhang Y, Zeng GM, Tang L, Chen J, Zhu Y, He XX, et al. Electrochemical sensor based on electrodeposited graphene-Au modified electrode and nanoAu carrier amplified signal strategy for attomolar mercury detection. *Anal Chem.* 2015;87(2):989–96. <https://doi.org/10.1021/ac503472p>.
 20. Chiu DT, deMello AJ, Di Carlo D, Doyle PS, Hansen C, Maceiczkyk RM, et al. Small but perfectly formed? Successes, challenges, and opportunities for microfluidics in the chemical and biological sciences. *Chem.* 2017;2(2):201–23. <https://doi.org/10.1016/j.chempr.2017.01.009>.
 21. Sachdeva S, Davis RW, Saha AK. Microfluidic point-of-care testing: commercial landscape and future directions. *Front Bioeng Biotechnol.* 2020;8:602659. <https://doi.org/10.3389/fbioe.2020.602659>.
 22. Fernández-la-Villa A, Pozo-Ayuso DF, Castaño-Álvarez M. Microfluidics and electrochemistry: an emerging tandem for next-generation analytical microsystems. *Curr Opin Electrochem.* 2019;15:175–85. <https://doi.org/10.1016/j.coelec.2019.05.014>.
 23. Kudr J, Zitka O, Klimanek M, Vrba R, Adam V. Microfluidic electrochemical devices for pollution analysis—a review. *Actuator B-Chem.* 2017;246:578–90. <https://doi.org/10.1016/j.snb.2017.02.052>.
 24. Ferreira F, Catalao KA, Mesquita RBR, Rangel A. New microfluidic paper-based analytical device for iron determination in urine samples. *Anal Bioanal Chem.* 2021;413(30):7463–72. <https://doi.org/10.1007/s00216-021-03706-9>.
 25. Moschou EA, Nicholson AD, Jia G, Zoval JV, Madou MJ, Bachas LG, et al. Integration of microcolumns and microfluidic fractionators on multitasking centrifugal microfluidic platforms for the analysis of biomolecules. *Anal Bioanal Chem.* 2006;385(3):596–605. <https://doi.org/10.1007/s00216-006-0436-z>.
 26. Zhu Y, Meng X, Chen Y, Li J, Shao H, Lu Y, et al. Self-served and fully automated biochemical detection of finger-prick blood at home using a portable microfluidic analyzer. *Actuator B-Chem.* 2020; 303. <https://doi.org/10.1016/j.snb.2019.127235>.
 27. Tombelli S, Trono C, Berneschi S, Berrettoni C, Giannetti A, Bernini R, et al. An integrated device for fast and sensitive immunosuppressant detection. *Anal Bioanal Chem.* 2021. <https://doi.org/10.1007/s00216-021-03847-x>.
 28. Hong Y, Wu M, Chen G, Dai Z, Zhang Y, Chen G, et al. 3D printed microfluidic device with microporous Mn_2O_3 -modified screen printed electrode for real-time determination of heavy metal ions. *ACS Appl Mater Interfaces.* 2016;8(48):32940–7. <https://doi.org/10.1021/acsami.6b10464>.
 29. Sun Q, Wang J, Tang M, Huang L, Zhang Z, Liu C, et al. A new electrochemical system based on a flow-field shaped solid electrode and 3D-printed thin-layer flow cell: detection of Pb^{2+} ions by continuous flow accumulation square-wave anodic stripping voltammetry. *Anal Chem.* 2017;89(9):5024–9. <https://doi.org/10.1021/acs.analchem.7b00383>.
 30. Han M, Uk Yoo B, Kim M, Lee J-Y, Hwan Lee K, Ho Park Y, et al. In-line detection of Cu+-related species in aged Cu plating bath using flow cell-based electrochemical method. *J Electroanal Chem.* 2021; 900. <https://doi.org/10.1016/j.jelechem.2021.115696>.
 31. Huang A, Li H, Xu D. An on-chip electrochemical sensor by integrating ITO three-electrode with low-volume cell for on-line determination of trace Hg(II). *J Electroanal Chem.* 2019; 848. <https://doi.org/10.1016/j.jelechem.2019.113189>.
 32. Perju A, Wongkaew N. Integrating high-performing electrochemical transducers in lateral flow assay. *Anal Bioanal Chem.* 2021;413(22):5535–49. <https://doi.org/10.1007/s00216-021-03301-y>.
 33. Mitchell KR, Esene JE, Woolley AT. Advances in multiplex electrical and optical detection of biomarkers using microfluidic devices. *Anal Bioanal Chem.* 2021. <https://doi.org/10.1007/s00216-021-03553-8>.
 34. Munir A, Zhu Z, Wang J, Zhou HS. FEM analysis of magnetic agitation for tagging biomolecules with magnetic nanoparticles in a microfluidic system. *Actuator B-Chem.* 2014;197:1–12. <https://doi.org/10.1016/j.snb.2014.01.120>.
 35. Dickinson E, Ekström H, Fontes E. COMSOL Multiphysics®: finite element software for electrochemical analysis. A mini-review. *Electrochem Commun.* 2014;40:71–4. <https://doi.org/10.1016/j.elecom.2013.12.020>.
 36. Wu ZQ, Du WB, Li JY, Xia XH, Fang Q. Establishment of a finite element model for extracting chemical reaction kinetics in a micro-flow injection system with high throughput sampling. *Talanta.* 2015;140:176–82. <https://doi.org/10.1016/j.talanta.2015.03.051>.
 37. Nielsen AV, Beauchamp MJ, Nordin GP, Woolley AT. 3D printed microfluidics. *Annu Rev Anal Chem (Palo Alto Calif).* 2020;13(1):45–65. <https://doi.org/10.1146/annurev-anchem-091619-102649>.
 38. Ogishi K, Osaki T, Morimoto Y, Takeuchi S. 3D printed microfluidic devices for lipid bilayer recordings. *Lab Chip.* 2022. <https://doi.org/10.1039/D1LC01077H>.

39. Ding X, Li Z, Liu C. Monolithic, 3D-printed lab-on-disc platform for multiplexed molecular detection of SARS-CoV-2. *Actuator B-Chem.* 2022;351:130998. <https://doi.org/10.1016/j.snb.2021.130998>.
40. Li F, Zheng Y, Yang M, Zhang Y, Pu Q. A triple-layer microchannel array chip with micro through-holes for smartphone based point-of-care testing of biomarker. *Actuator B-Chem.* 2022; 351. <https://doi.org/10.1016/j.snb.2021.130963>.
41. Bonfil Y, Brand M, Kirowaeisner E. Characteristics of subtractive anodic stripping voltammetry of Pb and Cd at silver and gold electrodes. *Anal Chim Acta.* 2002;464(1):99–114. [https://doi.org/10.1016/S0003-2670\(02\)00489-0](https://doi.org/10.1016/S0003-2670(02)00489-0).
42. Sabatino DR, Smith CR. Boundary layer influence on the unsteady horseshoe vortex flow and surface heat transfer. *ASME J Turbomach.* 2009;131(1):011015. <https://doi.org/10.1115/1.2813001>.
43. Stroock AD, Dertinger SK, Ajdari A, Mezic I, Stone HA, Whitesides GM. Chaotic mixer for microchannels. *Science.* 2002;295(5555):647–51. <https://doi.org/10.1126/science.1066238>.
44. Kuan DH, Wang IS, Lin JR, Yang CH, Huang CH, Lin YH, et al. A microfluidic device integrating dual CMOS polysilicon nanowire sensors for on-chip whole blood processing and simultaneous detection of multiple analytes. *Lab Chip.* 2016;16(16):3105–13. <https://doi.org/10.1039/C6LC00410E>.
45. Hajji H, Kolsi L, Hassen W, Al-Rashed AAAA, Borjini MN, Aichouni MA. Finite element simulation of antigen-antibody transport and adsorption in a microfluidic chip. *Physica E.* 2018;104:177–86. <https://doi.org/10.1016/j.physe.2018.07.034>.
46. Kondo K, Uno K, Shinohara K, et al. Shape evolution of electrodeposited copper bumps. *J Electrochem Soc.* 1996;143(6):1880–5. <https://doi.org/10.1149/1.1836919>.
47. Hinatsu JT. Diffusion coefficients for copper (II) in aqueous cupric sulfate-sulfuric acid solutions. *J Electrochem Soc.* 1989;136(1):125–32. <https://doi.org/10.1149/1.209671>.

Publisher's note Springer Nature remains neutral with regard to jurisdictional claims in published maps and institutional affiliations.